The Astrophysical Journal Letters, 869:L48 (9pp), 2018 December 20 https://doi.org/10.3847/2041-8213/aaedae
© 2018. The American Astronomical Society. All rights reserved.

The Disk Substructures at High Angular Resolution Program (DSHARP). VIII. The Rich Ringed Substructures in the AS 209 Disk

Viviana V. Guzmán[1,2], Jane Huang[3], Sean M. Andrews[3], Andrea Isella[4], Laura M. Pérez[5], John M. Carpenter[1], Cornelis P. Dullemond[6], Luca Ricci[7], Tilman Birnstiel[8], Shangjia Zhang[9], Zhaohuan Zhu[9], Xue-Ning Bai[10], Myriam Benisty[11,12], Karin I. Öberg[3], and David J. Wilner[3]

[1] Joint ALMA Observatory, Avenida Alonso de Córdova 3107, Vitacura, Santiago, Chile
[2] Instituto de Astrofísica, Ponticia Universidad Católica de Chile, Av. Vicuña Mackenna 4860, 7820436 Macul, Santiago, Chile
[3] Harvard-Smithsonian Center for Astrophysics, 60 Garden Street, Cambridge, MA 02138, USA
[4] Department of Physics and Astronomy, Rice University, 6100 Main Street, Houston, TX 77005, USA
[5] Departamento de Astronomía, Universidad de Chile, Casilla 36-D, Santiago, Chile
[6] Zentrum für Astronomie, Heidelberg University, Albert Ueberle Str. 2, D-69120 Heidelberg, Germany
[7] Department of Physics and Astronomy, California State University Northridge, 18111 Nordhoff Street, Northridge, CA 91130, USA
[8] University Observatory, Faculty of Physics, Ludwig-Maximilians-Universität München, Scheinerstr. 1, D-81679 Munich, Germany
[9] Department of Physics and Astronomy, University of Nevada, Las Vegas, 4505 South Maryland Parkway, Las Vegas, NV 89154, USA
[10] Institute for Advanced Study and Tsinghua Center for Astrophysics, Tsinghua University, Beijing 100084, People's Republic of China
[11] Unidad Mixta Internacional Franco-Chilena de Astronomía, CNRS/INSU UMI 3386, Departamento de Astronomía, Universidad de Chile, Camino El Observatorio 1515, Las Condes, Santiago, Chile
[12] Univ. Grenoble Alpes, CNRS, IPAG, F-38000 Grenoble, France

Received 2018 October 8; revised 2018 October 26; accepted 2018 October 29; published 2018 December 26

Abstract

We present a detailed analysis of the high angular resolution (0.″037, corresponding to 5 au) observations of the 1.25 mm continuum and ^{12}CO 2 − 1 emission from the disk around the T Tauri star AS 209. AS 209 hosts one of the most unusual disks from the Disk Substructures at High Angular Resolution Project sample, the first high angular resolution Atacama Large Millimeter Array survey of disks, as nearly all of the emission can be explained with concentric Gaussian rings. In particular, the dust emission consists of a series of narrow and closely spaced rings in the inner ∼60 au, two well-separated bright rings in the outer disk, centered at 74 and 120 au, and at least two fainter emission features at 90 and 130 au. We model the visibilities with a parametric representation of the radial surface brightness profile, consisting of a central core and seven concentric Gaussian rings. Recent hydrodynamical simulations of low-viscosity disks show that super-Earth planets can produce the multiple gaps seen in AS 209 millimeter continuum emission. The ^{12}CO line emission is centrally peaked and extends out to ∼300 au, much farther than the millimeter dust emission. We find axisymmetric, localized deficits of CO emission around four distinct radii, near 45, 75, 120, and 210 au. The outermost gap is located well beyond the edge of the millimeter dust emission, and therefore cannot be due to dust opacity and must be caused by a genuine CO surface density reduction, due either to chemical effects or depletion of the overall gas content.

Key words: dust, extinction – protoplanetary disks – techniques: high angular resolution

1. Introduction

The distribution of gas and dust in protoplanetary disks will directly impact the outcome of planetary systems (Weidenschilling 1977; Öberg et al. 2011). Characterizing the spatial distribution of both the dust and gas in disks is therefore essential to understanding how and what kind of planets can form. The main problem that theoretical models currently have is the fast migration of mm-sized dust particles toward the central star, preventing the formation of planetesimals, especially at larger distances from the star (Takeuchi & Lin 2002, 2005; Brauer et al. 2007, 2008). The solution that has been invoked to solve this problem is the presence of local pressure maxima that can stop, at least temporarily, the migration of solid particles and concentrate them for enough time to allow them to grow and form larger bodies (e.g., Pinilla et al. 2012). High angular resolution Atacama Large Millimeter Array (ALMA) observations of the millimeter dust continuum emission have shown evidence of such substructures in a handful of disks around nearby young stars, including HL Tau (ALMA Partnership et al. 2015), HD 163296 (Isella et al. 2016), TW Hya (Andrews et al. 2016), Elias 24 (Cieza et al. 2017; Dipierro et al. 2018), and AS 209 (Fedele et al. 2018). All of these disks present multiple ring/gap structures, and demonstrate the presence of mm-sized grains out to radii of at least 100 au in the disks. The origin of these ring-like substructures is unclear. The most favored mechanisms include planet-disk interactions (e.g., Dong & Fung 2017), radial pressure variations due to zonal flows in magnetohydrodynamic (MHD) turbulent disks (Johansen et al. 2009), and snowline-induced gaps (Zhang et al. 2015).

While the presence of substructures seems common, a larger sample of disks is needed to fully characterize the prevalence and configuration of such substructures, and constrain the physical or chemical processes responsible for them. This is the motivation of the Disk Substructures at High Angular Resolution Project (DSHARP), one of the large programs carried out with the ALMA in Cycle 4. The goal of the project is to characterize in a homogeneous way the substructures of 20 nearby protoplanetary disks, by mapping the 240 GHz dust continuum emission at a resolution of 35 mas, corresponding to 5 au (Andrews et al. 2018). One of the main outcomes of this survey is that bright rings and relatively faint gaps are an extremely common feature of disks, but the configuration (position and contrast) of the rings varies substantially from source to source (Huang et al. 2018a).

In this Letter we focus on one of the most unusual DSHARP sources, the disk around the classical T Tauri star AS 209. The large number of rings, the narrowness of the rings, and the wide gaps in the outer disk make AS 209 especially intricate compared to the vast majority of disks observed at high angular resolution. The star is located to the northeast of the main Ophiuchus star-forming region, at a distance of 121 ± 2 pc (Gaia Collaboration et al. 2018). The star has a spectral type K5, a mass of 0.9 $M_{\odot}$, and an age of 1.6 Myr (see Table 1 in Andrews et al. 2018). Observations at different wavelengths clearly show the effect of radial drift of larger grains, as the emission is noticeably more compact at longer wavelengths (Pérez et al. 2012; Tazzari et al. 2016). The surface density profile has been characterized with 870 μm observations at 0.″3 angular resolution (Andrews et al. 2009). More recently, Fedele et al. (2018) presented ALMA observations of the disk at ∼0.″17 angular resolution. The emission was characterized by a bright central component and the presence of two weaker dust rings near 75 and 130 au, and two gaps near 62 and 103 au. No obvious substructure was observed in the inner 60 au disk, except for a kink around 20–30 au. Fedele et al. (2018) also presented hydrodynamical simulations and found that the gap near 100 au located between the two outer rings could be produced by a Saturn-like planet.

The disk has also been observed in molecular line emission. Huang et al. (2016) presented observations of the three main CO isotopologues at 0.″6 angular resolution. While the emission from the most abundant isotopologue, ^{12}CO, was found to be centrally peaked and decreasing monotonically with radius, the ^{13}CO and C^{18}O emission showed evidence of an outer ring or bump centered at 150 au, near the millimeter dust edge.

In this Letter we present 1.25 mm dust continuum and ^{12}CO 2−1 line observations in the AS 209 disk. The observations and data reduction are presented in Section 2. The results of the dust continuum emission and the ^{12}CO line emission are described in Section 3. A discussion is presented in Section 4, and a summary is given in Section 5.

2. Observations

The observations presented here are part of the DSHARP ALMA Large Program (2016.1.00484.L). The AS 209 disk was observed with ALMA in Band 6 in 2017 September in configurations C40-8/9. Shorter baselines were observed in 2017 May in configuration C40-5. We use additional archival data from projects 2013.1.00226 (Huang et al. 2016) and 2015.1.00486.S (Fedele et al. 2018) that provide information on shorter and intermediate baselines, respectively.

A detailed description of the observations and data reduction process can be found in Andrews et al. (2018). Briefly, we first self-calibrated the short baselines, and in a second step self-calibrated the combined observations of short and long baselines. The continuum observations were cleaned in `CASA` 5.1, using the multi-scale option and a robust parameter of −0.5. A taper with FWHM of 37 mas × 10 mas and position angle (PA) of 162° was used to minimize point spread function (PSF)-related artifacts. The resulting continuum image has a beam of 38 mas × 36 mas, PA of 68°, and a rms noise of 19 μJy beam^{-1}.

The solutions of the continuum self-calibration were then applied to the ^{12}CO data. The molecular line data was first regridded to channels of 0.35 km s^{-1} and then cleaned with a robust parameter of 1.0. A Keplerian mask was used to help the cleaning process. The resulting ^{12}CO image has a beam of 95 mas × 70 mas, PA of 97° and a rms noise of 0.8 mJy beam^{-1} per channel.

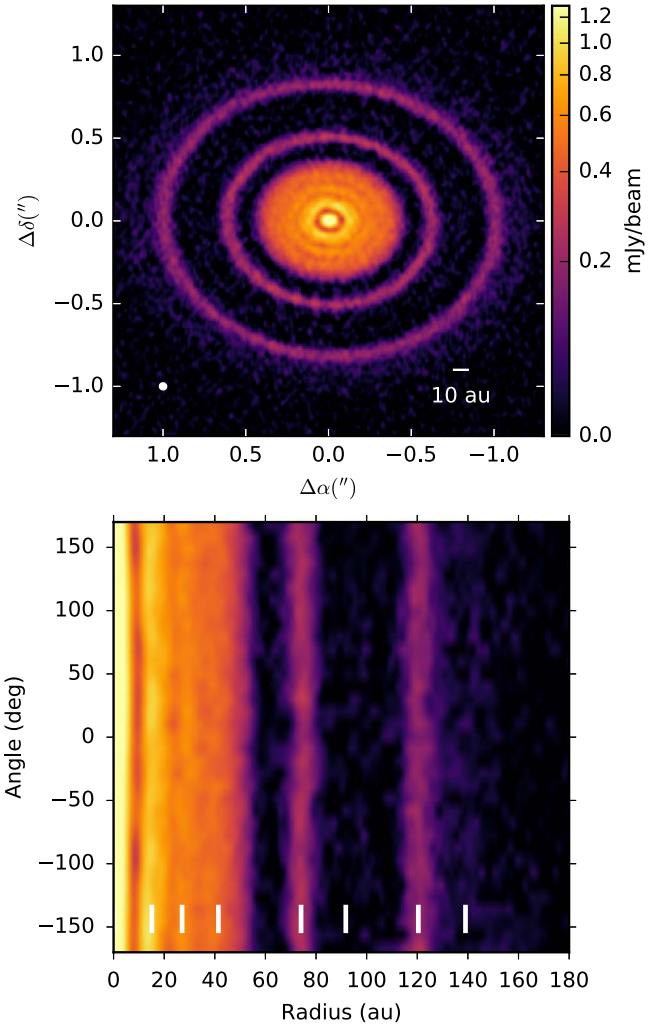

Figure 1. Dust continuum emission map (upper panel), and the deprojected emission shown in polar coordinates (bottom panel), using an inclination of 34.°88 and a position angle of 85.°76. The beam of 0.″03 × 0.″04 is shown in the bottom left, corresponding to a spatial resolution of 3.6 × 4.8 au. The white vertical bars in the bottom panel locate the position of the rings.

3. Results

In this section we first describe the main features of the dust continuum emission and model the surface brightness in the *uv*-plane to extract the positions, widths, and amplitudes of the different ring components. We then describe the spatial distribution of the ^{12}CO emission and its relation to the dust continuum emission.

3.1. Dust Continuum Emission

The image of the 1.25 mm dust continuum emission from the AS 209 disk is shown in Figure 1. The map is shown in the upper panel, while the lower panel shows the emission in polar coordinates to better visualize the axisymmetric nature of the emission. To create the map in polar coordinates, the image is first deprojected using an inclination of 34.°88 and a PA of 85.°76 (see section 3.1.1). The polar angle increases in the

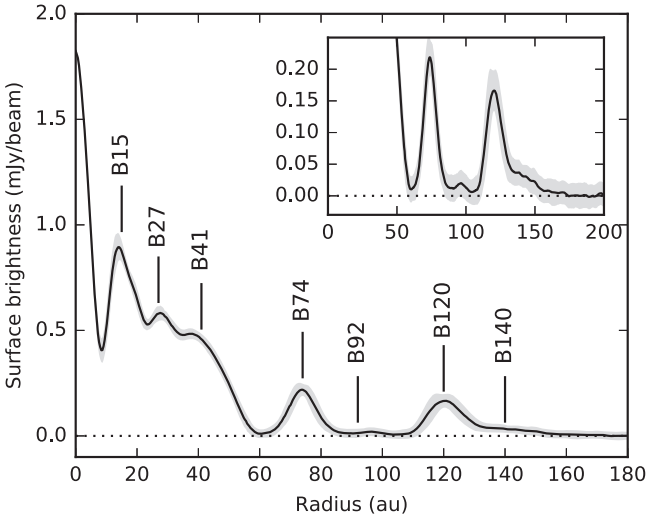

Figure 2. Deprojected azimuthally averaged radial profile of the dust continuum emission. An inset is shown in the upper-right panel to see the faint emission. The gray ribbon shows the standard deviation at each radius, and the vertical bars show the location of the rings given by our best-fit model.

clockwise direction, where zero degrees corresponds to the minor axis of the disk in the south direction. The dust emission is characterized *almost entirely* by a series of concentric narrow rings and gaps. Although the emission looks very axisymmetric, we cannot exclude the possibility that the rings have a small eccentricity ($e < 0.15$; see discussion in Huang et al. 2018a; Zhang et al. 2018). Figure 2 shows the deprojected azimuthally averaged emission profile, assuming the same inclination and PA mentioned above. The emission is centrally peaked and the surface brightness at the peak of the rings decreases with radius. A striking aspect of the emission is the difference between the inner 60 au disk, which consists of a central component and three closely packed rings, and the outer >60 au disk that consists of two bright rings that are well separated and spatially resolved. The two outer rings have been previously reported by Fedele et al. (2018). The new higher angular resolution observations reveal that the inner disk is not smooth but contains substantial substructure. In the inner disk the ring peaks are clearly resolved, but they overlap at lower surface brightnesses. The gap near 100 au is not completely empty of emission, as a faint ring can be seen in the deprojected radial profile around this radius (better seen in the zoomed panel in Figure 2). An additional faint component can also be seen at the edge of the disk, just outside the bright ring located at ∼120 au.

In the next section, we model the emission in the *uv*-plane to obtain the deconvolved position and width of the various rings observed in the disk.

3.1.1. Model Fitting in the uv-plane

Given the striking ring nature of the dust continuum emission, we modeled the radial brightness distribution with the sum of concentric Gaussian rings:

$$I(r) = \sum_{i=0}^{N} A_i \exp(-(r - r_i)^2/2\sigma_i^2). \quad (1)$$

The number of rings is chosen through visual inspection of the cleaned emission map and the deprojected radial profile (see Figures 1 and 2). We include a central component and three rings in the inner (<60 au) disk and four rings in the outer disk. The center position of the innermost Gaussian is fixed to zero, i.e., the disk center. Two of the outer rings correspond to the faint components near 100 and 130 au. We assume that the emission is axisymmetric, and create synthetic visibilities given by the Hankel transform (Pearson 1999)

$$V(\rho) = 2\pi \int_0^\infty I_\nu(r) J_0(2\pi\rho r) r dr \quad (2)$$

where ρ is the deprojected *uv*-distance in units of $k\lambda$, r is the radial angular distance from the disk center in units of radians, and J_0 is the zeroth-order Bessel function of the first kind.

To speed up the fitting method, the observed visibilities are first deprojected, radially averaged, and binned. We include *uv*-points from 10 to 10,000 kλ, in steps of 10 kλ. The inclination (i), PA, and center of the disk, given by an offset (δ_x, δ_y), are included as free parameters in the fit. The total number of free parameters is then 27; that is, 23 for the Gaussian rings (A_i, r_i, σ_i with i from 1 to 8; $r_0 = 0$) and 4 for the disk geometry (i, PA, δ_x, δ_y).

We use the affine invariant Markov chain Monte Carlo (MCMC) sampler implemented in the `emcee` package (Foreman-Mackey et al. 2013) to explore the parameter space. Table 1 summarizes the resulting best-fit parameters, calculated from the 50th percentile. The uncertainties are calculated from the 16th and 84th percentiles.

We find a disk inclination of 34°.9 and a PA of 85°.8, which are consistent with previous estimates (Fedele et al. 2018). These are also consistent with what Huang et al. (2018a) finds by fitting rings directly to the cleaned image. We also find a small offset from the phase center. We note that this offset is a just a nuisance parameter, as the disk center has been altered during the self-calibration process. The rings in the inner disk are centered at 15, 27, 41 au, and have FWHM between 7 and 17 au. Given that the spatial resolution of the observations is 5 au, the rings are all resolved. The two prominent rings in the outer disk are located at 74 and 120 au. Fedele et al. (2018) found this second ring to be located at 130 au instead of 120 au.

Table 1
Best-fit Parameters

Disk Geometry			
i (deg)	PA (deg)	δ_x (mas)	δ_y (mas)
$34.883^{+0.0151}_{-0.0042}$	$85.764^{+0.0184}_{-0.0061}$	$1.699^{+0.0003}_{-0.0006}$	$-3.102^{+0.0006}_{-0.0003}$
Gaussian Components			
Ring Name[a]	Rel. Amp[b]	r_i (au)	FWHM (au)
B0	$1.000^{+0.0024}_{-0.0027}$	0.00	$6.69^{+0.01}_{-0.01}$
B15 (B14)	$0.274^{+0.0005}_{-0.0012}$	$15.13^{+0.02}_{-0.03}$	$7.41^{+0.03}_{-0.01}$
B27 (B28)	$0.133^{+0.0014}_{-0.0012}$	$27.07^{+0.02}_{-0.03}$	$11.72^{+0.05}_{-0.03}$
B41 (B38)	$0.115^{+0.0001}_{-0.0001}$	$41.42^{+0.05}_{-0.03}$	$17.40^{+0.03}_{-0.06}$
B74 (B74)	$0.074^{+0.0003}_{-0.0002}$	$74.08^{+0.02}_{-0.01}$	$7.34^{+0.01}_{-0.01}$
B92 (B99)	$0.004^{+0.0001}_{-0.0001}$	$91.76^{+0.14}_{-0.09}$	$23.39^{+0.06}_{-0.08}$
B120 (B120)	$0.051^{+0.0003}_{-0.0002}$	$120.42^{+0.02}_{-0.02}$	$9.84^{+0.02}_{-0.03}$
B140 (B141)	$0.008^{+0.0001}_{-0.0001}$	$139.06^{+0.07}_{-0.08}$	$23.10^{+0.08}_{-0.16}$

Notes.
[a] The name in parenthesis corresponds to the one adopted in Huang et al. (2018a).
[b] Amplitudes are normalized to A_0, so that $I_{\rm norm}(r) = I(r)/A_0$. The normalization factor is given by $A_0 = F_{\rm tot} \big/ (2\pi \int_0^\infty I_{\rm norm}(r) J_0(0) r dr)$, where $F_{\rm tot}$ is the disk integrated flux density ($F_{\rm tot} \equiv V(\rho = 0) = 0.27$ Jy).

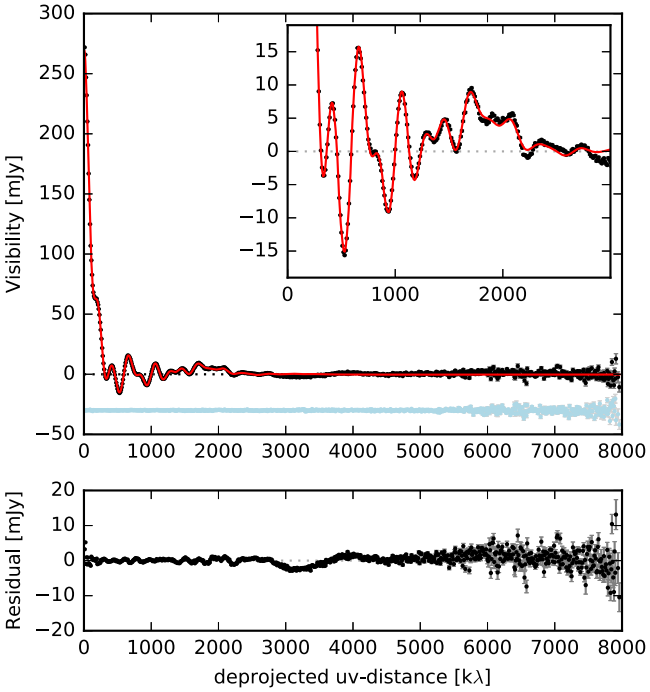

Figure 3. Deprojected and radially averaged visibilities. The real part of the visibilities is shown in black, and the imaginary part is shown in light blue (shifted to −30 mJy). The best-fit model is shown in red. An inset is shown in the upper-right corner.

The difference is due to the presence of another much fainter ring or bump, which we find to be located at 140 au. The faint ring located in between the two prominent outer rings is located at 92 au. We note that this ring is not located at the gap center but is instead closer to the inner ring near 74 au. These two fainter rings in the outer disk are found to be much broader (FWHM of 23 au) than the rest of the rings, in particular the two prominent outer rings that have FWHM of ∼7–10 au. This suggests that the nature of these components may be different from the rest, and their distribution is thus not well represented by a Gaussian. They could instead be treated as faint emission that is somehow connected to the brighter neighbor rings.

Figure 3 shows the observed real part of the deprojected visibilities in black, using the best-fit disk inclination and PA. The imaginary part of the visibilities are shown in light blue (shifted by −30 mJy), and remain close to zero for all *uv*-distance, consistent with symmetric emission of the disk. A zoom of the shorter-baseline visibilities is shown in the upper-right panel of the figure. Our simple parametric model of pure Gaussian rings can recover most of the (very complicated) structure seen in the radially averaged visibility profile. The cleaned image of the best-fit model is shown in the left panel of Figure 4. A slightly hexagonal structure and bumpiness can be seen in the rings, which is also seen in the observations. This demonstrates that these structures are not real, but correspond to PSF effects (see Andrews et al. 2018, for a discussion). The residuals, corresponding to the cleaned image of residual visibilities ($V_{\rm obs} - V_{\rm model}$), are shown in the right panel of the figure. Our best-fit model successfully reproduces the observations as seen by the low-level emission in the residuals map. However, some residuals remain near the disk center. This suggests that some additional substructure, in addition to Gaussian rings, are needed to fully reproduce the inner disk structure.

3.2. ^{12}CO $J = 2 - 1$ Emission

Figure 5 shows the moment-zero map of the ^{12}CO $J = 2 - 1$ line, integrated from −3 to 14 km s^{-1}. Pixels with a signal-to-noise ratio (S/N) lower than 3 have been clipped to highlight the substructure of the emission. The west side of the disk is moderately affected by cloud contamination due to the overlap between the velocities of the cloud with the blueshifted part of disk line emission. This explains the east–west asymmetry. The bottom panel in Figure 5 displays the azimuthally averaged deprojected profile, including only the east side of the disk. A selection of channel maps, showing the emission from the east side of the disk is shown in Figure 6. Channel maps for the full-velocity range can be found in Figure 7. The ^{12}CO $J = 2 - 1$ emission (1) is centrally peaked, (2) extends much farther out than the millimeter dust emission (out to 300 au), and (3) presents four main gaps or emission decrements in the outer disk, near 45, 75, 120, and 210 au. We note that this is not an effect of the clipping in the creation the moment-zero map, as the gaps are also seen with even more clarity in the individual channels (see Figure 6). The first gap is located very close to the edge of the inner millimeter disk. The next two gaps near 74 and 120 au spatially coincide with the two prominent outer dust rings. This gap is better seen in the channel maps, at a velocity of 5.8 km s^{-1}. The spatial coincidence of these two gaps with the location of the millimeter dust rings suggests that the rings are optically thick and are absorbing the ^{12}CO emission (see the discussion in section 4.2). The fourth and outermost gap seen in the ^{12}CO emission is located at a distance of 210 au from the central star, well beyond the millimeter dust edge. Therefore, it cannot be explained by dust opacity and must be a real decrease in the ^{12}CO column density at this radius.

The high angular resolution observations of the ^{12}CO $J = 2 - 1$ line allow us to determine the absolute orientation of the disk geometry (Rosenfeld et al. 2013). Because the ^{12}CO line is optically thick and the disk is flared, the observed emission originates from the surface layers of the disk that are elevated with respect to the midplane, where the dust continuum emission arises. At high enough angular resolution, and if the disk is inclined enough, it is possible to differentiate the front and back side of the disk. In the case of AS 209, the southern part of the disk appears to be closer to us, because the emission arising from the half-cone that is pointing toward us is shifted to the north and appears brighter. By contrast, the emission arising from the half-cone that is pointing to the back appears dimmer and is shifted to the south (see Figure 6). This effect is best seen at velocities of 5.8 and 6.15 km s^{-1}. Compared to other disks, such as IM Lup (Huang et al. 2018b) and HD 163296 (Isella et al. 2018), these effects are subtle, however, which is likely due to the higher inclinations of both disks compared to AS 209.

Scattered light observations trace the illumination of the small grains in the disk. It is useful to compare scattered light to ^{12}CO observations as they both trace the upper layers of the disk. The scattered light image of AS 209 presented recently by Avenhaus et al. (2018) was found to be very faint and featureless in comparison to other disks of similar mass. Although the scattered light is faint, it is detected out to a radius of 200 au. The faint nature of the scattered light could be the result of shadowing of the outer disk by one of the rings in the inner disk, most likely the one observed in millimeter continuum near 15 au. Another possibility is that the disk has

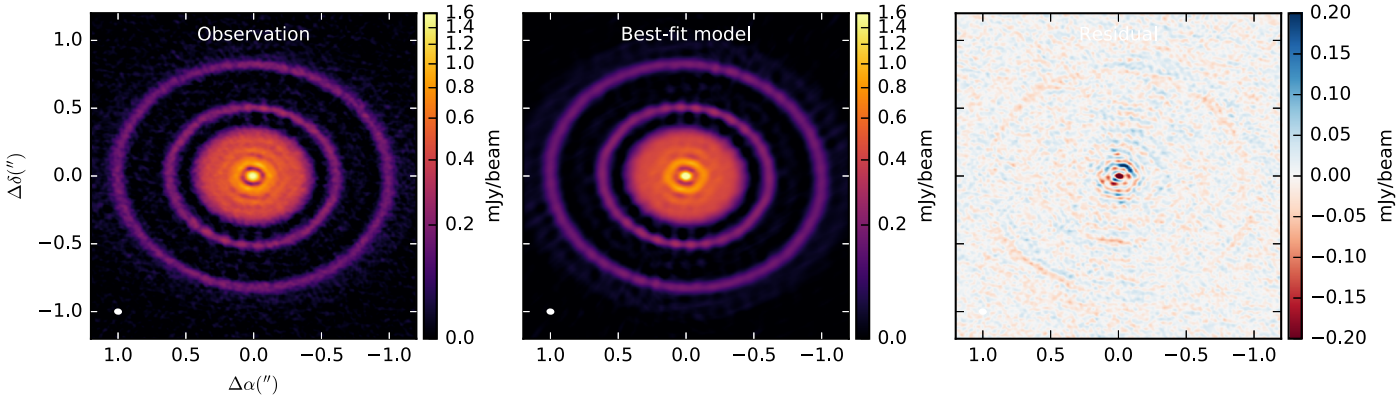

Figure 4. Observed dust continuum emission (left panel), best-fit model (middle panel) and residual (right panel) maps. The residuals are shown in linear scale.

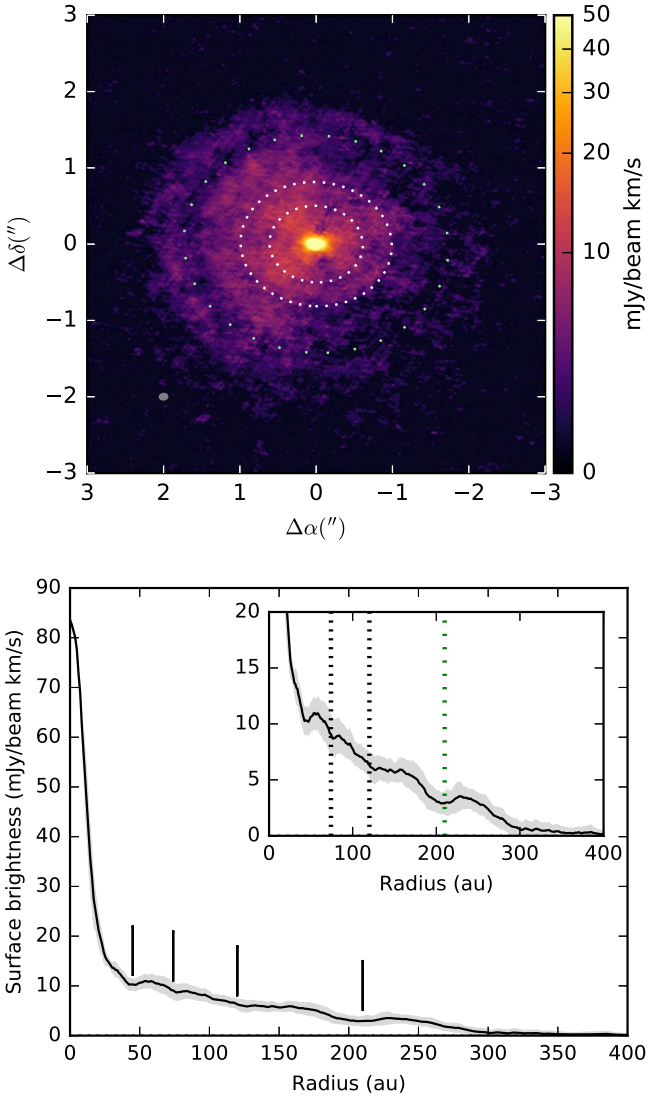

Figure 5. Moment-zero map (top panel) and azimuthally averaged deprojected radial profile (bottom panel) of the ^{12}CO $2-1$ line emission. Emission with S/N lower than 3 has been clipped. Only the uncontaminated east part of the image was considered to create the deprojected profile. The four vertical bars mark the position of the CO gaps. The two white (black in the lower panel) dotted lines mark the position of the prominent outer dust rings, located at 75 and 120 au, and the green dotted line marks the position of the outermost CO gap near 210 au.

experienced substantial settling and it is very flat, which hampers the efficient scattering of photons from the star. From these observations, the authors computed the deprojected profiles for two possible scenarios in which the north and the south part of the disk are closer to us. As explained above, the new ^{12}CO observations demonstrate that the latter alternative is the correct one. For this scenario, the resulting radial profile of the scattered light emission presents three rings, two of them located near the two prominent outer dust rings seen by ALMA, and a third one near 250 au. They also find a gap near 200 au. This outer ring and gap coincide with the gap and outer ring seen in the ^{12}CO emission.

4. Discussion

Although other disks are known to harbor multiple rings in their millimeter emission, the disk around AS 209 is unique because of the striking difference between the substructure in the inner and outer disk, and the symmetric nature of the rings. While the inner disk consists of closely packed rings that resemble the emission seen in TW Hya and HD 163296, the outer disk harbors two prominent rings that are separated by a gap with a much higher contrast compared to the other disks. In this section we discuss the different possible origins for these substructures, in both the dust continuum and the ^{12}CO line emission.

4.1. Origin of the Dust Emission Ring Morphology

One of the main results from the DSHARP Large Program is that rings and gaps are very common in protoplanetary disks (Huang et al. 2018a), but the origin of these substructures is still unknown. Several hypotheses have been proposed, the most popular being the presence of planets. An embedded planet can induce a gap opening (or multiple gaps) by dynamic interactions with the disk. The depth of the gap will depend on several factors, including the mass of the planet, the time that the planet has had to carve the gap, the disk aspect ratio h/r, and the disk viscosity—planets will open deeper gaps in low-viscosity disks (e.g., Crida et al. 2006; Bae et al. 2017; Dong & Fung 2017). Using 3D hydrodynamical simulations, Fedele et al. (2018) found that the position, width, and depth of the outermost gap at 100 au in the AS 209 disk is consistent with the presence of a $0.2\,M_{\rm J}$ planet located at 95 au. Their simulation also predicted the presence of a feature inside the

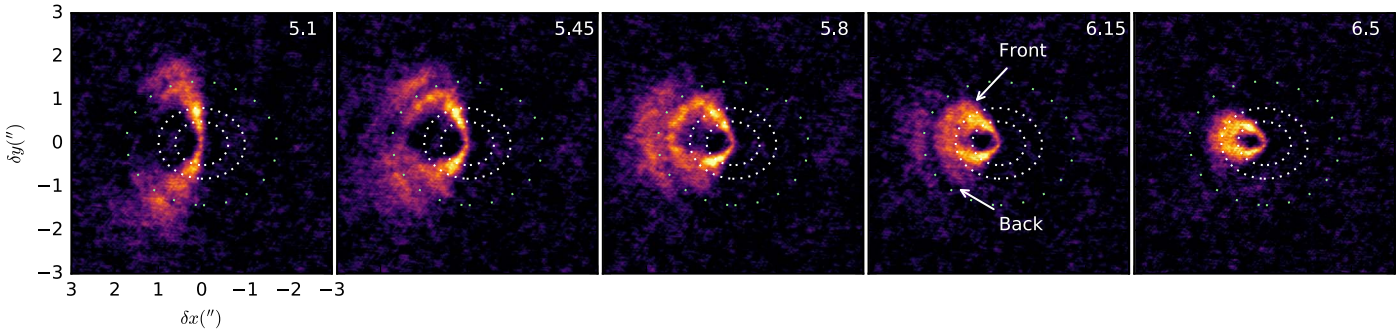

Figure 6. Channel maps of the ^{12}CO $2-1$ line emission. Only channels from the uncontaminated east side of the disk are shown. The velocity of each channel is shown in top-right corner. The two inner ellipses (dotted lines) mark the position of the two brighter outer dust rings located at 74 and 120 au. A third ellipse (green dotted line) corresponding to a projected radius of 210 au is also drawn, to mark the position of a gap of CO emission in the outer disk.

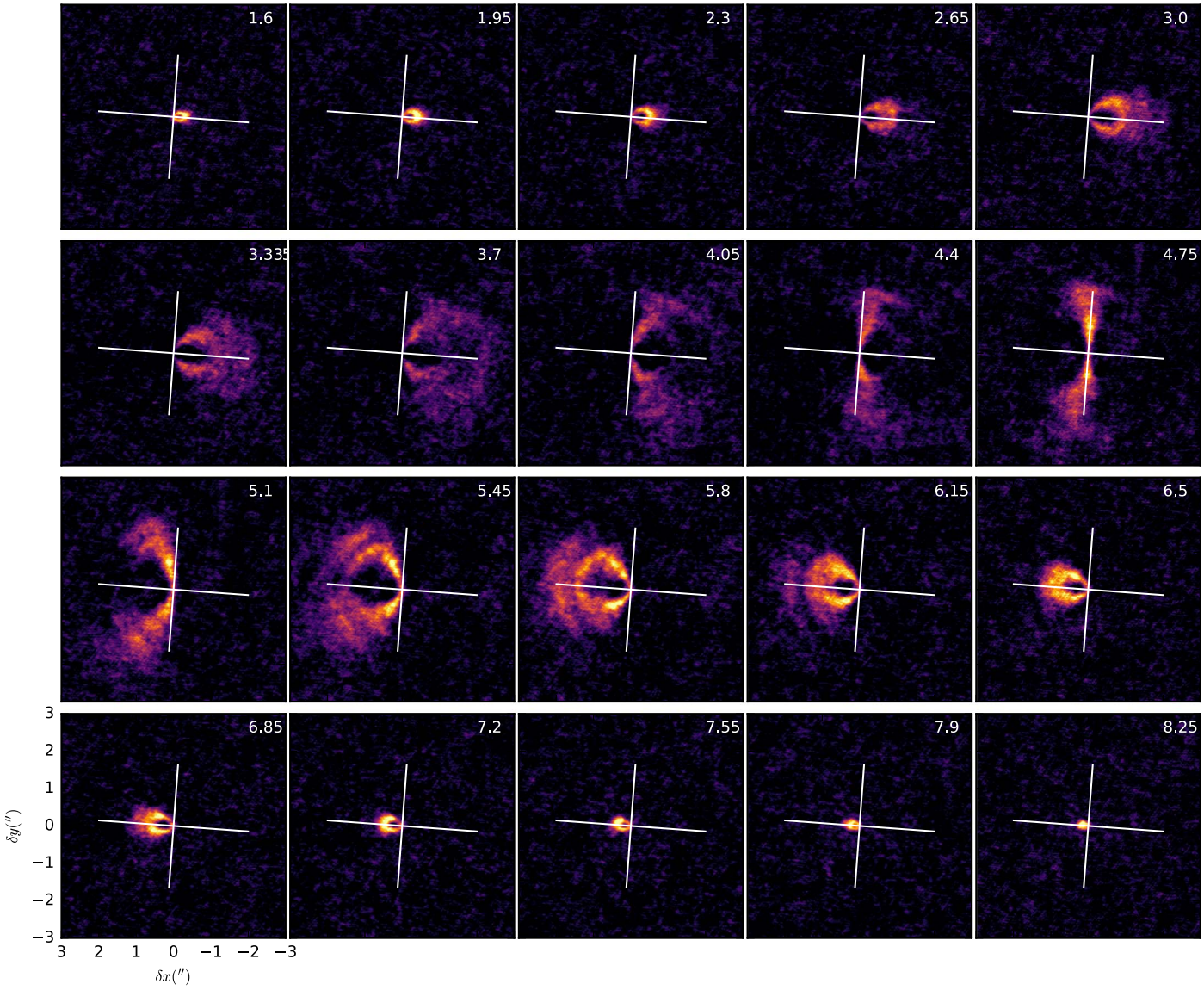

Figure 7. Channel maps of the ^{12}CO $2-1$ line emission. The velocity of each channel is shown in the top-right corner. The major and minor axis are shown in white.

gap. The feature was not detected in their observations, but it is now detected with the DSHARP observations. Fedele et al. (2018) also found that the same planet could produce the other prominent gap in the continuum at 60 au. Alternatively, Dong et al. (2018) showed that a $\sim$0.1 $M_{\rm J}$ planet located at 80 au can produce the two major gaps seen in the outer AS 209 disk (at 60 and 100 au), and predicted an additional gap near 40 au, which is now detected by DSHARP. Another possibility, also

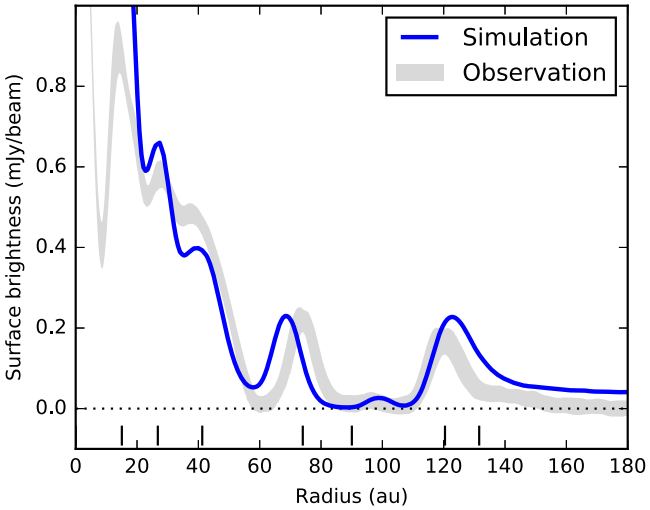

Figure 8. Hydrodynamical simulation showing the gaps induced in a disk by the presence of a planet orbiting at 99 au from the star, overlaid on the observed radial profile in AS 209. A detailed description of the simulation is given in Zhang et al. (2018).

consistent with the observations, is the presence of a second $\sim 0.1\,M_{\rm J}$ planet in the inner gap at 57 au, close to a 2:1 resonance with the outer planet (Fedele et al. 2018).

The higher angular resolution observations reveal the presence of additional gaps in the inner disk that were unresolved in the $\sim 0\farcs17$ resolution observations of Fedele et al. (2018). Although they did not resolve the three individual rings in the inner disk, they did report a kink in the profile near 20–30 au. The multiple rings seen in the inner disk could be produced by planets in the outer disk. Hydrodynamical simulations have shown that a single super-Earth planet could produce major gaps both interior of the planet location and in the outer disk (e.g., Bae et al. 2017; Dong et al. 2017). A particular new feature in the AS 209 disk is the gap located at roughly 10 au. The gap is not resolved and it is not seen in the scattered light image, perhaps because it is hidden by the $0\farcs185$ coronagraph (Avenhaus et al. 2018). Inspired by the disk structures observed in the DSHARP sources, Zhang et al. (2018) presented a grid of hydrodymical simulations. In particular for AS 209, they show that a single planet located at 99 au could produce simultaneously the various rings seen in the inner 60 au and outer disk in AS 209 if α varies radially. The simulation is shown in Figure 8. The planet responsible for the gaps has a mass of $0.087\,M_{\rm J}$. Quite remarkably, this simulation is able to produce not only the large gap near 100 au, but also matches the position of the gaps in the inner disk, at 60au, 35 au, and even the one at 24 au. A detailed description of the simulation, as well as a synthetic image of the dust continuum emission, is given in Zhang et al. (2018).

It is worth noting that the most prominent gaps seen in the dust continuum are not seen as prominent features in the ^{12}CO emission (but see Section 4.2). This does not rule out the planet hypothesis, as theoretical simulations have shown that it is possible for planets to open gaps in the dust while leaving the gas emission relatively featureless (Paardekooper & Mellema 2004; Isella et al. 2016; Rosotti et al. 2016; Dipierro & Laibe 2017), especially for optically thick lines like ^{12}CO. This is particularly true if the planet has a low mass, which is the case for the putative planets in the AS 209 disk (Zhang et al. 2018).

It has also been suggested that the rings observed at millimeter wavelengths could by produced by changes in the dust properties at the location of snowlines of the main ices, like H_2O, NH_3, CO, and N_2 (Zhang et al. 2015; Okuzumi et al. 2016). In this scenario, material can be concentrated at the location of condensation fronts, which is critical for the formation of planetesimals. At these locations the μm-sized and mm-sized dust particles would have grown to cm sizes and larger, and would thus be invisible at millimeter wavelengths, appearing as gaps in the observations. We can estimate the location of these snowlines in the AS 209 disk, using the midplane temperature derived by Andrews et al. (2009). The two outer gaps in the disk, near 60 and 100 au, have temperatures of 20 and 15 K, which are comparable to the condensation temperatures of pure ^{12}CO and N_2 ices, respectively (Zhang et al. 2015). The water snowline, which is supposed to be the most efficient snowline to concentrate solids, is located very close to the central star (<2 au), and is thus unresolved even with the ALMA observations. It is worth remembering that gas temperatures in disks are very uncertain. In particular, for the AS 209 disk the gas temperature was derived by fitting a power law to lower angular resolution observations of the dust continuum (Andrews et al. 2009). The location of snowlines could therefore be shifted in the disk. A major problem with this scenario is that the gaps in the AS 209 disk are very wide (almost 20 au for the outermost gap) and also very depleted in dust. Although they may contribute some toward the formation of these gaps, it is hard to explain how condensation fronts alone could produce such wide gaps. Moreover, dust coagulation and disk evolution models that take into account the condensation and evaporation of major volatiles do not find enhanced grain growth near the ^{12}CO snowline (Stammler et al. 2017). Only at the location of the water snowline is dust growth found to be efficient enough to produce strong features in the dust continuum emission (Birnstiel et al. 2010; Drążkowska & Alibert 2017; Schoonenberg & Ormel 2017).

Other alternatives mainly involve internal disk gas dynamics resulting from the coupling between gas and magnetic field. These include zonal flows due to magnetorotational instability (MRI) turbulence (Johansen et al. 2009; Bai & Stone 2014; Simon & Armitage 2014), ring formation at dead-zone boundaries (Flock et al. 2015; Lyra et al. 2015), or through spontaneous magnetic flux concentration (Bai & Stone 2014; Béthune et al. 2017; Suriano et al. 2018). The zonal flow scenario generally produces radial density variations up to a few tens of percent on scales of a few scale heights. While this may be consistent with the rings found in TW Hya (Andrews et al. 2016), the ring separation in AS 209 is much broader (e.g., 46 au separation for disk scale height of 5–10 au in the outer disk), and the contrast between rings and gaps is also much larger. The dead-zone scenario relies on a specific location corresponding to a transition in the radial resistivity profile well within 100 au, making it difficult to reconcile with the widely separated multi-ring structure seen in the outer disk of AS 209. The last scenario offers large degrees of freedom attributed to how magnetic flux threading the disks evolve, though this process is very poorly understood, and existing studies largely rely on simplified assumptions (Lubow et al. 1994; Guilet & Ogilvie 2014; Okuzumi et al. 2014; Bai & Stone 2017). Therefore, while some scenarios are unlikely, better theoretical understandings

are needed to assess the possibility of magnetic origin for the substructures in AS 209.

4.2. Origin of the ^{12}CO $J = 2 - 1$ Emission Rings and Gaps

One way to produce gaps in the ^{12}CO emission is by optically thick dust emission. For a long time, dust opacity at millimeter wavelengths was thought to be negligible, at least in the outer disk. However, recent low-angular observations of a large sample of disks (Tripathi et al. 2017) as well as high angular resolution observations cast doubt on this assumption (see also the case of HD 163296; Isella et al. 2018). In the case of AS 209, the peak brightness temperature of the two prominent outer rings is ∼0.15–0.20 mJy, which corresponds to Rayleigh–Jeans brightness temperatures of ∼3–4 K, and would only produce an optical depth of ∼0.4–0.5 even assuming relatively conservative dust temperatures of ∼12–15 K (see also Dullemond et al. 2018). The dust rings therefore seem to be optically thin. One possible explanation for the decrease of ^{12}CO emission close to the location of these two dust rings is that the rings are not resolved and are clumpy in nature. A filling factor of one-third would be enough to reproduce the ratio between the dust temperature and the brightness temperature of the rings. Another possible explanation is that some emission was removed during the continuum subtraction process. Indeed, part of the continuum can be absorbed by the molecule at the line center, especially when the optical depth of the line is much higher than the optical depth of the continuum. This can lead to an overestimation of the dust contribution at the line center, which is estimated from the line-free channels, resulting in an underestimation of the line emission (see Boehler et al. 2017; Weaver et al. 2018).

Huang et al. (2016) presented CO isotopologue observations of the AS 209 disk at 0.″6 angular resolution, and found that the C^{18}O emission consists of a central peak and a ring component centered at a radius of ∼150 au. This ring component, however, was not observed in their optically thick ^{12}CO emission. The new higher angular resolution ^{12}CO observations reveal some new interesting substructure. In particular, we detect a fainter outer ring centered at ∼240 au, which was not detected in the C^{18}O emission probably due to the lower signal-to-noise of the emission in the outer disk. The CO distribution thus appears to have at least two ring components located outside the millimeter dust disk and also well outside the expected location of the CO snowline (between 30 and 90 au; Huang et al. 2016). Huang et al. (2016) suggested that the C^{18}O ring at 150 au is caused by CO being desorbed back into the gas phase, which could happen by some non-thermal process (cosmic rays or high-energy photons), or by thermal inversion due to dust migration (e.g., Cleeves 2016). However, the presence of a second ring at 240 au casts doubt on this interpretation. If chemistry is the cause of the outermost ^{12}CO ring, then the inner ring should be produced by a different mechanism. Another alternative is that the outermost gap near 210 au corresponds to a reduction of the total gas density at this location. The origin of this gap is unclear, but we can speculate that it is produced by a planet. The formation of planets this far from the star is hard to explain theoretically, but indirect evidence of their existence has been found. Pinte et al. (2018) found localized deviation from Keplerian velocities in the ^{12}CO emission, and attributed the observed velocity kink to a planet located ∼260 au from the young HD 163296 star. We do not detect any clear evidence of deviations from Keplerian velocities in the AS 209 disk, but this could be due to lower S/N and spectral resolution compared to the HD 163296 observations. Alternatively, the velocity kink could be present in the west side of the disk and thus hidden by the cloud contamination. We do not detect any localized emission from a circumplanetary disk at this radius in the dust continuum image either. Recently, Teague et al. (2018) presented a new method to measure rotation curves in disks. Using lower angular resolution archival CO data, they found deviations of up to 5 percent from Keplerian rotation at 250 au in the AS 209 disk.

5. Summary

We have presented observations of the 1.2 mm dust continuum and the ^{12}CO $2 - 1$ line emission from the disk around the classical AS 209 star, as part of the ALMA Large Program DSHARP. We have modeled the dust emission in the *uv*-plane and find that the emission can be well represented by a series of narrow concentric rings. In addition to the two prominent rings located at 74 and 120 au that were previously reported by Fedele et al. (2018), we find a central component and three rings in the inner <60 au disk. Two main gaps are seen, near 60 and 100 au. The second gap at 100 au is not completely empty from dust grains, however, as we detect faint dust emission within the gap. We also detect faint emission in the outer edge of the disk, out to ∼160 au.

The ^{12}CO image exhibits four gaps. Two of them spatially coincide with the position of the two prominent outer dust rings, which suggests that the rings are optically thick. The outermost ^{12}CO gap near ∼210 au is located well beyond the millimeter dust edge, and therefore traces real ^{12}CO depletion or a substantial decrease in the gas density.

We discuss the different possibilities for the origin of the gaps seen in the continuum emission. We find that, although some of the gaps roughly coincide with the location of snowlines of major volatiles, it it is unlikely that all the observed gaps are induced by a chemical effect. This is because of the varied structures observed in the different DSHARP sources, in terms of the width and contrast of the gaps, and snowlines should produce similar configurations (see Huang et al. 2018a, for a discussion). Recent hydrodynamical simulations show, however, that super-Earth planets can produce the various rings seen in the continuum image, both in the inner disk and in the outer disk. As the spatial resolution of the observations improve, revealing new features, the locations and masses of these planets can be better constrained. If the presence of a planet (or multiple planets) in the AS 209 disk is confirmed, then planet formation starts very early (few Myr) in the evolution of disks. Moreover, if a planet is responsible for the gap seen in CO at ∼210 au, then planets can form at large distance from the central star, which challenges our current understanding of the planet formation process.

V.V.G. and J.C. acknowledge support from the National Aeronautics and Space Administration under grant No. 15XRP15_20140 issued through the Exoplanets Research Program. S.A. and J.H. acknowledge funding support from the National Aeronautics and Space Administration under grant No. 17-XRP17_2-0012 issued through the Exoplanets Research Program. T.B. acknowledges funding from the

European Research Council (ERC) under the European Unions Horizon 2020 research and innovation programme under grant agreement No 714769. J.H. acknowledges support from the National Science Foundation Graduate Research Fellowship under grant No. DGE-1144152. L.R. acknowledges support from the ngVLA Community Studies program, coordinated by the National Radio Astronomy Observatory, which is a facility of the National Science Foundation operated under cooperative agreement by Associated Universities, Inc. Z.Z. and S.Z. acknowledges support from the National Aeronautics and Space Administration through the Astrophysics Theory Program with grant No. NNX17AK40G and Sloan Research Fellowship. Simulations are carried out with the support from the Texas Advanced Computing Center (TACC) at The University of Texas at Austin through XSEDE grant TG- AST130002. C.P.D. acknowledges support by the German Science Foundation (DFG) Research Unit FOR 2634, grants DU 414/22-1 and DU 414/23-1. M.B. acknowledges funding from ANR of France under contract number ANR-16-CE31-0013 (Planet Forming disks). L.P. acknowledges support from CONICYT project Basal AFB-17002 and from FCFM/U. de Chile Fondo de Instalación Académica. This Letter makes use of the following ALMA data: ADS/JAO.ALMA# 2016.1.00484.L, ADS/JAO.ALMA# 2013.1.00226 and ADS/JAO.ALMA# 2015.1.00486.S. ALMA is a partnership of ESO (representing its member states), NSF (USA) and NINS (Japan), together with NRC (Canada), NSC andASIAA (Taiwan), and KASI (Republic of Korea), in cooperation with the Republic of Chile. The Joint ALMA Observatory is operated by ESO, AUI/NRAO, and NAOJ.

Appendix

ORCID iDs

Viviana V. Guzmán https://orcid.org/0000-0003-4784-3040
Jane Huang https://orcid.org/0000-0001-6947-6072
Sean M. Andrews https://orcid.org/0000-0003-2253-2270
Andrea Isella https://orcid.org/0000-0001-8061-2207
John M. Carpenter https://orcid.org/0000-0003-2251-0602
Cornelis P. Dullemond https://orcid.org/0000-0002-7078-5910
Tilman Birnstiel https://orcid.org/0000-0002-1899-8783
Shangjia Zhang https://orcid.org/0000-0002-8537-9114
Zhaohuan Zhu https://orcid.org/0000-0003-3616-6822
Xue-Ning Bai https://orcid.org/0000-0001-6906-9549
Myriam Benisty https://orcid.org/0000-0002-7695-7605
David J. Wilner https://orcid.org/0000-0003-1526-7587

References

ALMA Partnership, Brogan, C. L., Pérez, L. M., et al. 2015, ApJL, 808, L3
Andrews, S. M., Huang, J., Pérez, L. M., et al. 2018, ApJL, 869, L41
Andrews, S. M., Wilner, D. J., Hughes, A. M., Qi, C., & Dullemond, C. P. 2009, ApJ, 700, 1502
Andrews, S. M., Wilner, D. J., Zhu, Z., et al. 2016, ApJL, 820, L40
Avenhaus, H., Quanz, S. P., Garufi, A., et al. 2018, arXiv:1803.10882
Bae, J., Zhu, Z., & Hartmann, L. 2017, ApJ, 850, 201
Bai, X.-N., & Stone, J. M. 2014, ApJ, 796, 31
Bai, X.-N., & Stone, J. M. 2017, ApJ, 836, 46
Béthune, W., Lesur, G., & Ferreira, J. 2017, A&A, 600, A75
Birnstiel, T., Dullemond, C. P., & Brauer, F. 2010, A&A, 513, A79
Boehler, Y., Weaver, E., Isella, A., et al. 2017, ApJ, 840, 60
Brauer, F., Dullemond, C. P., & Henning, T. 2008, A&A, 480, 859
Brauer, F., Dullemond, C. P., Johansen, A., et al. 2007, A&A, 469, 1169
Cieza, L. A., Casassus, S., Pérez, S., et al. 2017, ApJL, 851, L23
Cleeves, L. I. 2016, ApJL, 816, L21
Crida, A., Morbidelli, A., & Masset, F. 2006, Icar, 181, 587
Drążkowska, J., & Alibert, Y. 2017, A&A, 608, A92
Dipierro, G., & Laibe, G. 2017, MNRAS, 469, 1932
Dipierro, G., Ricci, L., Pérez, L., et al. 2018, MNRAS, 475, 5296
Dong, R., & Fung, J. 2017, ApJ, 835, 146
Dong, R., Li, S., Chiang, E., & Li, H. 2017, ApJ, 843, 127
Dong, R., Li, S., Chiang, E., & Li, H. 2018, arXiv:1808.06613
Dullemond, K., Birnstiel, T., Huang, J., et al. 2018, ApJL, 869, L46
Fedele, D., Tazzari, M., Booth, R., et al. 2018, A&A, 610, A24
Flock, M., Ruge, J. P., Dzyurkevich, N., et al. 2015, A&A, 574, A68
Foreman-Mackey, D., Conley, A., Meierjurgen Farr, W., et al. 2013, emcee: The MCMC Hammer, ascl:1303.002
Gaia Collaboration, Brown, A. G. A., Vallenari, A., et al. 2018, A&A, 616, A1
Guilet, J., & Ogilvie, G. I. 2014, MNRAS, 441, 852
Huang, J., Andrews, S. M., Dullemond, C. P., et al. 2018a, ApJL, 869
Huang, J., Andrews, S. M., Pérez, L. M., et al. 2018b, ApJL, 869, L43
Huang, J., Öberg, K. I., & Andrews, S. M. 2016, ApJL, 823, L18
Isella, A., Guidi, G., Testi, L., et al. 2016, PhRvL, 117, 251101
Isella, A., Huang, J., Andrews, S. M., et al. 2018, ApJL, 869, L49
Johansen, A., Youdin, A., & Klahr, H. 2009, ApJ, 697, 1269
Lubow, S. H., Papaloizou, J. C. B., & Pringle, J. E. 1994, MNRAS, 267, 235
Lyra, W., Turner, N. J., & McNally, C. P. 2015, A&A, 574, A10
Öberg, K. I., Murray-Clay, R., & Bergin, E. A. 2011, ApJL, 743, L16
Okuzumi, S., Momose, M., Sirono, S.-i., Kobayashi, H., & Tanaka, H. 2016, ApJ, 821, 82
Okuzumi, S., Takeuchi, T., & Muto, T. 2014, ApJ, 785, 127
Paardekooper, S.-J., & Mellema, G. 2004, A&A, 425, L9
Pearson, T. J. 1999, in ASP Conf. Ser. 180, Synthesis Imaging in Radio Astronomy II, A Collection of Lectures from the Sixth NRAO/NMIMT Synthesis Imaging Summer School, ed. G. B. Taylor et al. (San Francisco, CA: ASP), 335
Pérez, L. M., Carpenter, J. M., Chandler, C. J., et al. 2012, ApJL, 760, L17
Pinilla, P., Birnstiel, T., Ricci, L., et al. 2012, A&A, 538, A114
Pinte, C., Price, D. J., Ménard, F., et al. 2018, ApJL, 860, L13
Rosenfeld, K. A., Andrews, S. M., Hughes, A. M., Wilner, D. J., & Qi, C. 2013, ApJ, 774, 16
Rosotti, G. P., Juhasz, A., Booth, R. A., & Clarke, C. J. 2016, MNRAS, 459, 2790
Schoonenberg, D., & Ormel, C. W. 2017, A&A, 602, A21
Simon, J. B., & Armitage, P. J. 2014, ApJ, 784, 15
Stammler, S. M., Birnstiel, T., Panić, O., Dullemond, C. P., & Dominik, C. 2017, A&A, 600, A140
Suriano, S. S., Li, Z.-Y., Krasnopolsky, R., & Shang, H. 2018, MNRAS, 477, 1239
Takeuchi, T., & Lin, D. N. C. 2002, ApJ, 581, 1344
Takeuchi, T., & Lin, D. N. C. 2005, ApJ, 623, 482
Tazzari, M., Testi, L., Ercolano, B., et al. 2016, A&A, 588, A53
Teague, R., Bae, J., Birnstiel, T., & Bergin, E. 2018, arXiv:1810.04961
Tripathi, A., Andrews, S. M., Birnstiel, T., & Wilner, D. J. 2017, ApJ, 845, 44
Weaver, E., Isella, A., & Boehler, Y. 2018, ApJ, 853, 113
Weidenschilling, S. J. 1977, Ap&SS, 51, 153
Zhang, K., Blake, G. A., & Bergin, E. A. 2015, ApJL, 806, L7
Zhang, Z., Zhu, Z., Huang, J., et al. 2018, ApJL, 869, L47